Proceedings of the 4th International Conference on Mathematical Physics and Computational Simulation
DOI: 10.54254/2753-8818/2026.33935

Study on the Mechanism of Wall-Driven Cyclone Separation Process and Its Enhanced Removal of PM2.5 Particles

Xiwei Qiu

WLSA Shanghai Academy, Shanghai, China
qiuxiweidsb@163.com

Abstract. This study focuses on indoor PM2.5 pollution control needs and innovatively proposes a curved wall geometry regulation strategy to enhance cyclone separation performance. By establishing a parametric design method based on conic curve eccentricity (e=0.2~1.8), systematic models of cyclone separators with convex, straight, and concave conical segments were constructed. Combining Box-Behnken experimental design with computational fluid dynamics simulation (using RSM turbulence model coupled with DPM discrete phase tracking), the study deeply revealed the enhancement mechanism of curved wall geometry on particulate removal processes. Results indicate that the convex structure (e=1.8) demonstrates optimal performance in fine particle capture and energy consumption control, achieving over 50% particle size classification efficiency for 1μm particles (15% higher than straight cone type) while significantly reducing pressure drop. The concave structure (e=0.2) exhibits higher total separation efficiency across all concentration conditions, offering>85% efficiency at the cost of 10-15% pressure drop increase. Mechanistic analysis confirms that curved walls optimize radial force balance by effectively regulating internal flow field tangential velocity distribution, turbulence kinetic energy dissipation characteristics, and particle motion trajectories (e.g., significantly extending fine particle retention time), thereby effectively suppressing short-circuit flow phenomena. This research provides new insights for developing efficient and low-consumption household air purification technologies.Theoretical basis and design ideas.

Keywords: cyclone separation technology, curved wall optimization, fine particulate matter capture, computational fluid dynamics Introduction

1. Introduction

1.1. Research background

Accelerated urbanization and industrialization have made complex air pollution a persistent public health issue, with PM2.5 posing significant risks due to its ability to carry toxic substances and penetrate the alveolar–blood barrier. China's GB/T 18883-2022 standard tightens the PM2.5 limit from 0.075 mg/m³ to 0.05 mg/m³ (33.3% reduction) [1], marking a shift toward precise indoor pollution control. Indoor sources are increasingly diverse, with secondhand smoke contributing about 32% [2] and emerging pollutants such as microplastics and pathogenic spores rising [3]. While

HEPA filters achieve 99.97% efficiency [4], their cost and maintenance limit adoption; the "cyclone separation + filtration" approach reduces pressure drop by about 58% [5], offering a more efficient and cost-effective solution (see Figure 1).

Figure 1. The cyclone separator in Dyson Vacuum Cleaner

Cyclone separators, widely used in industry due to their simple structure and low cost, achieve gas–solid separation through centrifugal forces and boundary layer velocity gradients. This study targets PM2.5 control in household environments and establishes a "design–simulation–validation" framework. By introducing curved-wall geometry to regulate particle motion, the cyclone structure is optimized using curvature design, CFD simulation, and 3D-printed experiments, while response surface analysis balances separation efficiency and pressure drop. The results demonstrate that the proposed method enhances performance while reducing operational and maintenance costs, providing a feasible approach for applying cyclone separation in household air purification.

1.2. Current research status at home and abroad

Cyclone separators, as a type of swirling flow separation technology, can achieve high-efficiency micron-scale particle separation without chemical additives, featuring simple structure and strong adaptability. However, limitations such as high energy loss, asymmetric flow, bypass effects, and wall erosion persist [6, 7], necessitating geometric optimization [8]. Among them, the cylinder–cone cyclone is the most widely used, and the cone profile plays a crucial role: compared with linear designs, curved profiles improve flow stability and reduce particle mixing. During separation, particles are mainly influenced by centrifugal force, radial pressure gradient force, and fluid drag (see Fig.2), with centrifugal and pressure gradient forces being dominant. The radial force formula for particles in cyclone separators is detailed in Table 1.

$$F_{\sum} = F_B - F_C - F_D \pm F_M \tag{1}$$

Table 1. Radial force of particles in cyclone separator(Eqs.2-5)

Force name	Formula	Direction	number
$\mathrm{F_C}$	$F_C = m\frac{v_t^2}{r} = \frac{\pi\rho_p D_p^3 \frac{v_t^2}{r}}{6}$	Opposite to the axis	(2)
$\mathrm{F_B}$	$F_B = v_p\rho_f\frac{v_t^2}{r} = \frac{\pi D_p^3 v_t^2}{6r}\rho_f$	To the axis	(3)
$\mathrm{F_D}$	$F_D = 3\pi D_P \mu \nu_r$	Opposite to the axis	(4)
$\mathrm{F_M}$	$F_M = k\rho_f D_p^3 \omega v_r$	Determined by the direction of autorotation	(5)

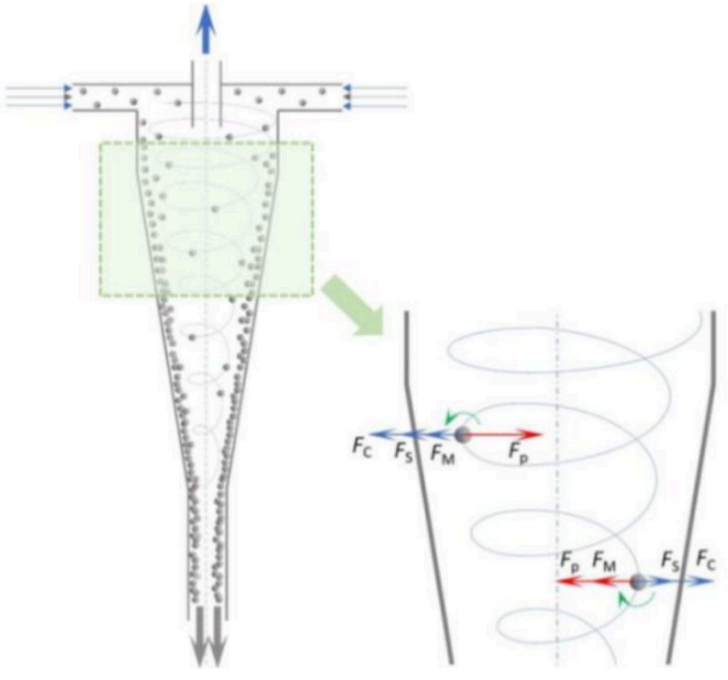

Figure 2. Schematic diagram of radial force of particles in cyclone

Straight-type cyclone separators are widely used due to their simple structure and ease of fabrication, including single-cone and multi-cone designs [9]. Studies show that smaller cone angles or double-cone configurations improve separation efficiency [10-11]. With advances in 3D printing and numerical simulation, curved-profile cyclones have emerged, employing convex, concave, and composite curves (e.g., parabolic [12], hyperbolic [13], elliptical [14], three-stage [15], and high-order curves [16]) to optimize flow fields and balance pressure drop and efficiency: convex designs reduce pressure drop by 12%–15%, while concave designs increase 5 μm particle capture efficiency up to 92% [17]. Studies also indicate that different curve types significantly affect performance, with convex designs reducing pressure drop, concave designs improving efficiency, and parabolic profiles outperforming linear ones, enabling 5 μm particle classification [18-19]. Overall, cyclone design is evolving from single to multi-cone, linear to curved, and simple to high-order composite geometries. Meanwhile, CFD simulations (e.g., RSM or LES) and response surface methods enable detailed flow analysis and structural optimization, further enhancing separation performance [20-21].

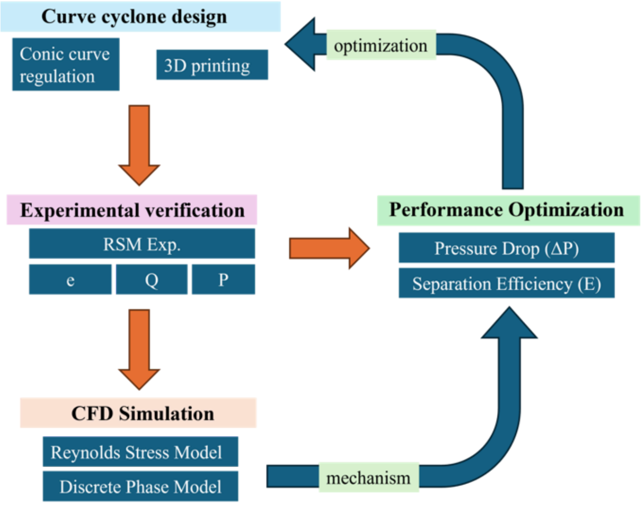

Figure 3. Research technical route

In summary, the curved conical wall significantly affects cyclone performance; CFD, response surface analysis, and 3D printing can optimize flow for efficient, low-energy separation. As shown in Fig.3, this study targets 0.1–10 μm microplastics and integrates flow control, simulation, experimentation, and optimization.

2. Design method of curve profile cyclone

2.1. Centrifugal force and curve concavity morphology

The cone wall geometry (concave, linear, convex) is a key parameter influencing tangential velocity, pressure gradient, and separation efficiency in cyclone separators. Based on conic section theory (see Fig.4), different cutting planes produce distinct curves: perpendicular to the axis yields a circle; intersecting one side forms an ellipse; parallel to the generatrix produces a parabola; and perpendicular to the base but offset from the axis results in a hyperbola. These curves provide a theoretical basis for curved wall optimization.

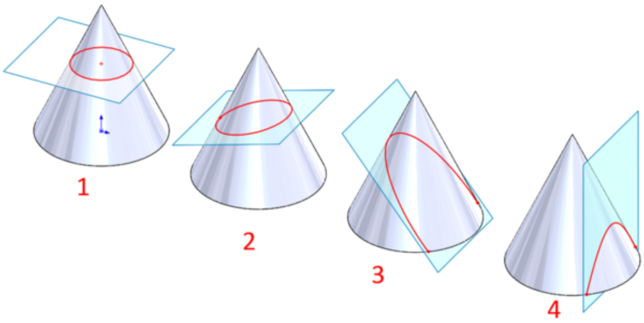

Figure 4. Several forms of conic curve

Based on conic section equations, the eccentricity e serves as the key parameter governing curve geometry and can systematically describe wall curvature. Taking the circle (e=0) as a reference, larger e indicates greater deviation from circular shape; e<1 corresponds to concave curves with deeper curvature at smaller values, while e>1 represents convex curves with increasing protrusion; e=1 reduces to a straight line. This provides a parametric design framework for precisely controlling the cone wall curvature in cyclone separators.

This study uses eccentricity e with linear interpolation to build parametric equations (Eqs.6–8), enabling controlled design of wall curvature.

$$x\left(t\right)=17.5\left(1-t\right)+4t+k\left(e\right)\cdot t\left(1-t\right)\cdot \varDelta x \tag{6}$$

$$z\left(t\right)=-35\left(1-t\right)-200t+k\left(e\right)\cdot t\left(1-t\right)\cdot \varDelta z \tag{7}$$

$$k\left(e\right)=0.5\cdot\left(e-1\right)\quad\left(where\ e\ ranges\ from\ 0.1\ to\ 2.0\right) \tag{8}$$

2.2. Parametric constraints and unified design method

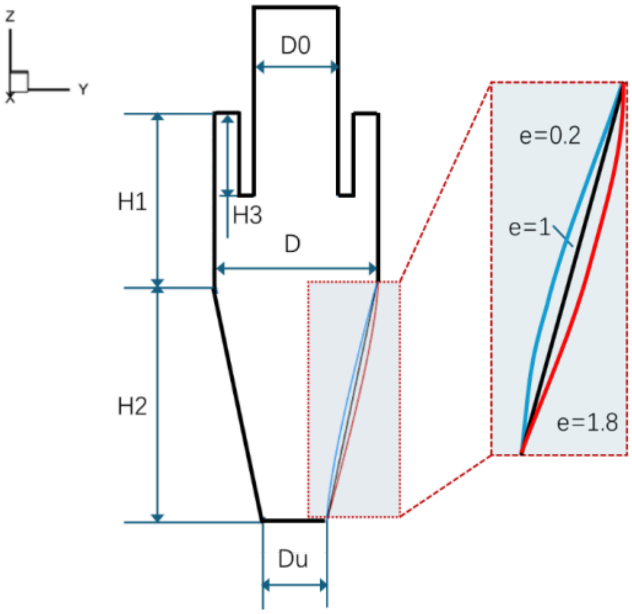

Figure 5. The geometry and dimension of the cone section

A unified parametric model is established based on endpoint constraints and monotonicity conditions: the start point (15.5, -31) and end point (5.8, -77) are fixed using linear terms -9.7t and -46t, while ensuring dx/dt < 0 throughout for monotonicity. Within this framework, a single parametric equation is used, and different curve shapes are generated by adjusting the eccentricity e. At $t=0.5$, $e=0.2$ yields $x=8.55$ (2.1 lower than linear), representing maximum concavity; $e=1.8$ gives $x=13.05$ (2.4 higher), representing maximum convexity; and $e=1$ reduces to a straight line (H2), as shown in Fig.5.

2.3. Design of curved cyclone

Cyclone optimization requires coordinated control of D , $\mathrm{H1}\ (\approx \mathrm{D})$, $\mathrm{H2}$, Do , $\mathrm{H3}$, Du, and inlet size ($\mathrm{a} \times \mathrm{b}$), see Table 2. The cone extends particle paths, while a smaller underflow enhances swirl for PM2.5 separation. Based on this, eccentricity e is introduced, and configurations with $\mathrm{e} = 0.2$ and $\mathrm{e} = 1.8$ form three cyclone models $(\mathrm{H1},\ \mathrm{H2},\ \mathrm{H3})$.

Table 2. Basic structural parameters of cyclone separator

Design parameter	D	H1	H2	H3	Do	Du	a	b
	mm	mm	mm	mm	mm	mm	mm	mm
value	31	31	31	50	15.5	11.6	5	12.5

3. Box Beckhen Design (BBD)

The Box–Behnken response surface method is a statistical multivariable optimization approach that fits a quadratic model through a closed loop of design, modeling, analysis, and optimization, suitable for balancing efficiency, cost, and safety. As a three-level incomplete factorial design, it samples edge midpoints of pairwise factor interactions with multiple center points (see Fig.6), avoiding extreme conditions while ensuring model stability. The number of experiments is $N = 2k(k-1) + C_0$; for $k = 3$, only 15 runs are required, significantly fewer than full factorial designs.

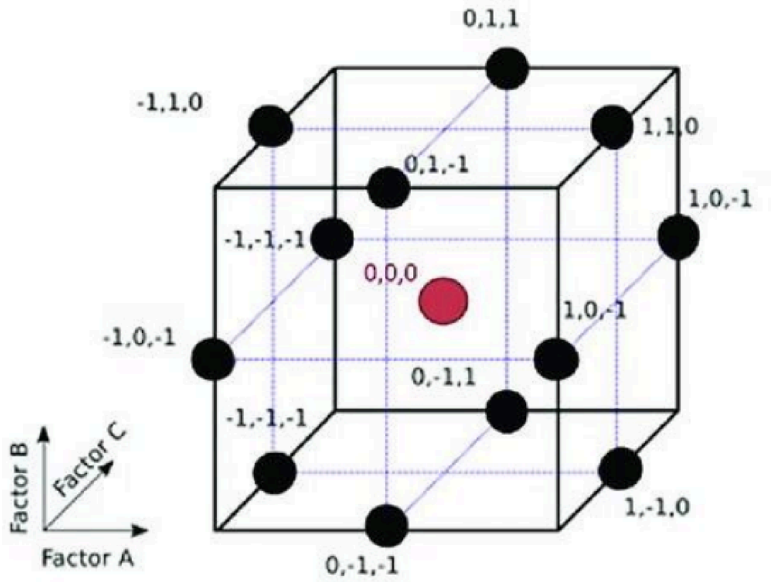

Figure 6. Box-Behnken design of experimental points

This study employs a Box–Behnken design to investigate the effects of eccentricity A (0.2, 1, 1.8), flow rate Q (30, 40, 50 L/min), and concentration C (1, 3, 5 g/L) on separation efficiency (E) and pressure drop (Pd), with 15 runs including repeated center points and randomized order. A quadratic response surface model $Y = \beta_0 + \sum \beta_i X_i + \sum \beta_{ii} X_i^2 + \sum \beta_i j X_i X_j + \varepsilon$ is used to fit the relationships, while ANOVA evaluates main and interaction effects (e.g., $\mathrm{A} \times \mathrm{Q}$). Response surface and contour plots are used for visualization and optimization.

Table 3. Box-Behnken experimental points

		Factor 1	Factor 2	Factor 3
Std	Run	A:e	B:Q	C:C
11	1	1	30	5
7	2	0.2	40	5
12	3	1	50	5
4	4	1.8	50	3
1	5	0.2	30	3
14	6	1	40	3
6	7	1.8	40	1
8	8	1.8	40	5
10	9	1	50	1
9	10	1	30	1
15	11	1	40	3
5	12	0.2	40	1
2	13	1.8	30	3
3	14	0.2	50	3
13	15	1	40	3

PE microplastic particles (density 1.05 g/cc) were selected as $PM_{2.5}$ surrogates, with particle sizes of d50 ≈ 5.02μm and d90 ≈ 10.127μm, representing fine and difficult-to-separate particles. The experimental setup (see Fig.7) includes a vortex blower (air supply), a 3D-printed cyclone separator (separation unit), and an electronic balance with 0.1 mg precision (filter weighing).

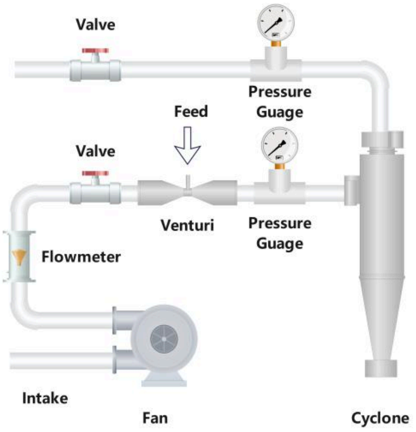

Figure 7. Experimental setup

In the experiment, inlet flow rates were set to 20, 40, and 60 L/min by adjusting the blower valve. After stabilization, microplastics were introduced at concentrations of 1, 3, and 5 g/L via a Venturi injector and uniformly dispersed into the cyclone. Key parameters such as pressure drop (Pd), flow rate, and collected mass were recorded. Separation efficiency was calculated from mass differences measured by an electronic balance. The data were then analyzed to evaluate the effects of flow rate and concentration, and a response surface model was developed to assess main and interaction effects. Finally, validation tests at selected conditions confirmed model reliability.

4. Establishment of numerical model

The cyclone separation process involves complex gas–solid multiphase flow. To accurately capture strong swirling turbulence, the Reynolds Stress Model (RSM) with a six-equation closure is employed to resolve anisotropic turbulence and predict turbulence generation, dissipation, and energy redistribution. The CFD simulation framework is shown in Fig.8.

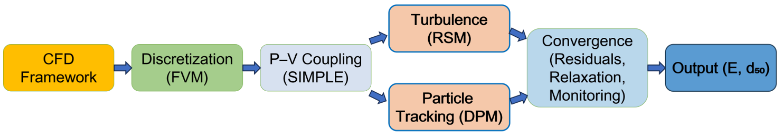

Figure 8. CFD simulation algorithm framework

4.1. RSM model

The Reynolds Stress Model (RSM) is an advanced turbulence model in ANSYS Fluent, known for accurately capturing anisotropic turbulence. For incompressible flow, the Reynolds stress transport equations can be expressed as Eqs. (9–10):

$$\begin{aligned}\frac{\partial}{\partial t}\left(\rho\overline{u_i^{'}u_j^{'}}\right)+\frac{\partial}{\partial x_k}\left(\rho u_k\overline{u_i^{'}u_j^{'}}\right)= & -\frac{\partial}{\partial x_k}\left[\rho\overline{u_i^{'}u_j^{'}u_k^{'}}+\overline{p^{'}\left(\delta_{kj}u_i^{'}+\delta_{ik}u_j^{'}\right)}\right]+\frac{\partial}{\partial x_k}\left[\mu\frac{\partial}{\partial x_k}\left(\overline{u_i^{'}u_j^{'}}\right)\right]\\ & -\rho\left(\overline{u_i^{'}u_j^{'}}\frac{\partial u_j}{\partial x_k}+\overline{u_j^{'}u_k^{'}}\frac{\partial u_i}{\partial x_k}\right)-\rho\beta\left(g_i\overline{u_j^{'}\theta}+g_j\overline{u_i^{'}\theta}\right)\\ & +p^{'}\left(\frac{\partial u_i^{'}}{\partial x_j}+\frac{\partial u_j^{'}}{\partial x_i}\right)-2\mu\frac{\partial u_i^{'}}{\partial x_k}\frac{\partial u_j^{'}}{\partial x_k}\\ & -2\rho\Omega_k\left(\overline{u_j^{'}u_m^{'}}\varepsilon_{jkm}+\overline{u_i^{'}u_m^{'}}\varepsilon_{jkm}\right)+S_{user}\end{aligned}\tag{9}$$

$$\begin{aligned}&\frac{\partial}{\partial \mathrm{t}}\left(\rho\overline{\rho u_{\mathrm{i}}^{'}u_{\mathrm{j}}^{'}}\right)+\frac{\partial}{\partial x_k}\left(\rho u_k\overline{u_{\mathrm{i}}^{'}u_{\mathrm{j}}^{'}}\right)\\ &=D_{T,ij}+D_{L,ij}+P_{ij}+G_{ij}+\varphi_{ij}+\varepsilon_{ij}+F_{ij}\end{aligned}\tag{10}$$

The equations are respectively the liquid density ρ , velocity u_i , velocity fluctuation $u_i^{'}$ and position length x_i . The turbulent diffusion term is $D_{T,ij}$, the molecular diffusion term is $D_{L,ij}$, the stress generating term is P_{ij} , the buoyancy generating term is G_{ij} , the pressure strain term is φ_{ij} , the dissipation term is ε_{ij} , and the system rotation term is F_{ij} .

4.2. Description of inter-particle forces and establishment of discrete phase model

In studying microplastic motion within a cyclone, particles are subjected to multiple forces that govern their interaction with the fluid, concentration distribution, and pressure drop. Therefore, it is necessary to systematically analyze the main forces acting on particles.

(1) Stokes obstruction

In solid–liquid two-phase flow, the relative velocity between particles and fluid is often small, allowing inertia to be neglected and the flow approximated as Stokes flow. In practice, the Stokes drag on particles is obtained via drag coefficients; for spherical particles, the corresponding drag model is applied in this study:

$$C_D = \left[0.63 + 4.8\left(\frac{Re_s}{V_{r,s}}\right)^{-0.5}\right]^2 \tag{11}$$

$$Re_s = \frac{\rho_f d_{s|\bar{v}_s-\bar{v}_f|}}{\mu_f}\,[34] \tag{12}$$

$$V_{r,s} = 0.5\Bigg(A - 0.06Re_s + \sqrt{(0.06Re_s)^2 + 0.12Re_s\,(2B - A) + A^2} \tag{13}$$

While $\alpha_f \leq 0.85$, A= ${\alpha_f}^{4.14}$, $B = 0.8{\alpha_f}^{1.28}$;while $\alpha_f > 0.85$, A= ${\alpha_f}^{4.14}$, $B = {\alpha_f}^{2.65}$.

(2) Pressure gradient force

The pressure gradient force is induced by the shape of the particles, manifesting as the pressure difference generated by the fluid flow in the axial direction of the spherical particles.

(3) Magnus force and Saffman force

The Magnus force arises from particle rotation-induced velocity differences and acts perpendicular to the rotation direction, while the Saffman force is generated by shear-induced velocity gradients and typically acts perpendicular to particle motion, producing lift when the upper velocity exceeds the lower. Although both are smaller than drag, they are considered in this study using a lift coefficient of $\mathrm{C_L} = 0.5$.

(4) Virtual mass force

When particles accelerate in a flow, the surrounding fluid is also accelerated, generating an effective "added mass," known as the virtual mass force . Its magnitude equals half the inertia of the displaced fluid moving with the same acceleration, corresponding to half the mass of the displaced fluid. This effect is negligible when particle density is much higher than fluid density but becomes significant when densities are comparable. In this study, it is incorporated via Eq. (14).

$$\mathrm{C_{vm}}\alpha_\mathrm{s}\rho_\mathrm{f}(\bar{\mathrm{v}}_\mathrm{f} \bullet \nabla\bar{\mathrm{v}}_\mathrm{f} - \bar{\mathrm{v}}_\mathrm{s} \bullet \nabla\bar{\mathrm{v}}_\mathrm{s}) \tag{14}$$

C_{vm} denotes the virtual mass force coefficient, with the default value adopted in this study.

(5) Particle-to-particle collisions

The force caused by the collision between particles is expressed by the following formula 15:

$$g_{0,ss} = \left[1 - \left(\frac{\alpha_s}{\alpha_{s,max}}\right)^{\frac{1}{3}}\right]^{-1} \tag{15}$$

where $g_{0,ss}$ denotes the collision probability between particles, and $\alpha_{s,max}$ represents the maximum allowable solid volume fraction in the slurry system. This parameter is generally determined experimentally, and $\alpha_{s,max} = 0.6$.

In addition to the forces mentioned above, particles are also subjected to gravity. Although the Basset force, related to the history of motion, may exist, it is negligible in this study because particles and fluid enter the cyclone with the same initial velocity; thus, it is not considered.

4.3. Geometry, meshing, and simulation conditions

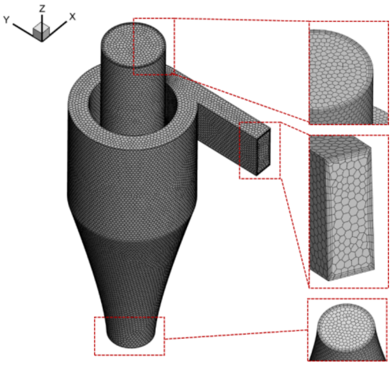

Figure 9. The cyclone and the detail of the boundary layer mesh

Three cyclone models were geometrically constructed and meshed in ANSYS Fluent. Grid independence was verified using five mesh sizes (110,254–1,258,453), and 358,562 hexahedral cells were selected as optimal when tangential velocity at z = -35 mm stabilized (see Fig.9). Simulations employed the RSM and DPM models: RSM captures turbulence anisotropy and energy evolution, while DPM tracks particle motion and phase interactions. This framework enables analysis of geometric effects on flow behavior and separation efficiency, supporting mechanism understanding and design optimization.

The simulation uses a velocity inlet (v = 15 m/s) and pressure outlets (zero back pressure) at both overflow and underflow, with sampling ports. Air is the continuous phase, and particles have a density of 1.2 g/mL with sizes from 0.5 to 8 μm (10 levels); both phases share the same inlet velocity. No-slip wall conditions are applied, with PRESTO pressure discretization, SIMPLE coupling, and QUICK schemes. Convergence is achieved when inlet–outlet flow balance is satisfied and residuals reach 1.0 × 10⁻⁵.

5. Results and discussion

5.1. Differential pressure

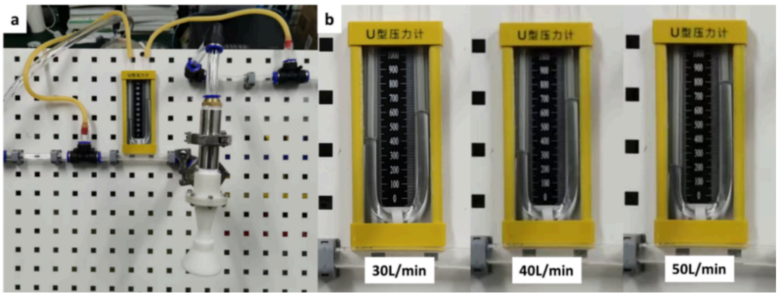

Figure 10. Diagram of cyclone separator (a) schematic of cyclone separator (b) pressure drop at different air velocities

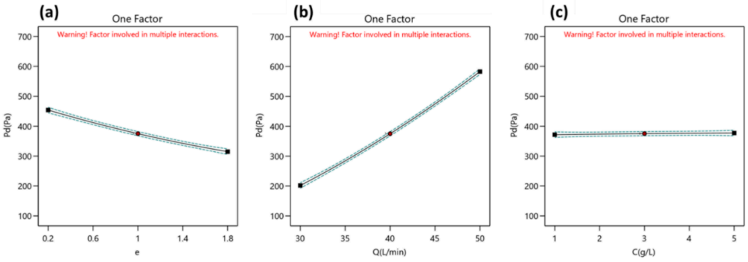

Figure 11. Pressure drop diagram of cyclone separator (a) effect of centrifugal speed (b) effect of flow rate (c) effect of concentration

A cyclone experimental setup was constructed (Fig. 10), using a vortex pump for airflow and a U-tube manometer to measure pressure drop. Results (Figs. 11–12) show that the convex type H3 has the lowest pressure drop, increasing quadratically with flow rate and about 20% lower than the straight cone under the same conditions; H2 is intermediate, with local high-pressure regions at cone transitions; H1 is highest, 10–15% above H2, indicating stronger flow confinement and energy consumption. Overall, particle concentration has a minor effect on pressure drop.

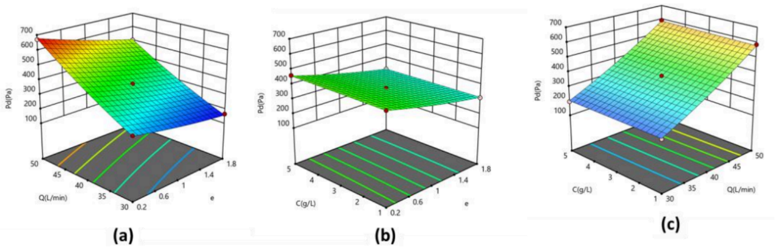

Figure 12. Pressure drop response surface plots (a) centrifugal velocity/flow rate (b) centrifugal velocity/concentration (c) flow rate/concentration

5.2. Separation efficiency

As shown in Figs. 13-14, response surface analysis indicates that the concave type H1 maintains a total separation efficiency above 85% at high concentrations, outperforming others due to extended residence time, stabilized swirl, and reduced bypass flow. The convex type H3 achieves over 75% efficiency, improving by 8–12% compared to the straight cone, by enhancing near-wall centrifugal forces, reducing secondary flow and back-mixing, and lowering turbulence dissipation. In contrast, the straight cone H2 suffers from flow separation and vortex core oscillation, leading to dead zones and reduced stability.

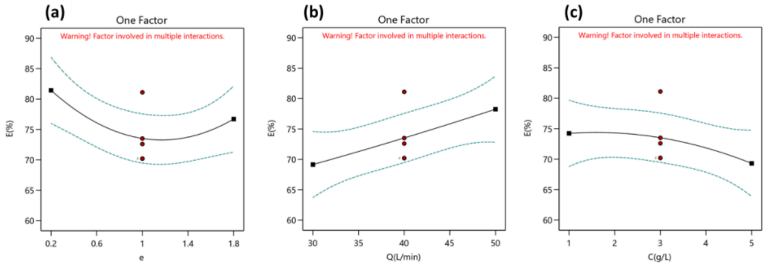

Figure 13. Single-factor analysis of separation efficiency (a) effect of centrifugal speed (b) effect of flow rate (c) effect of concentration

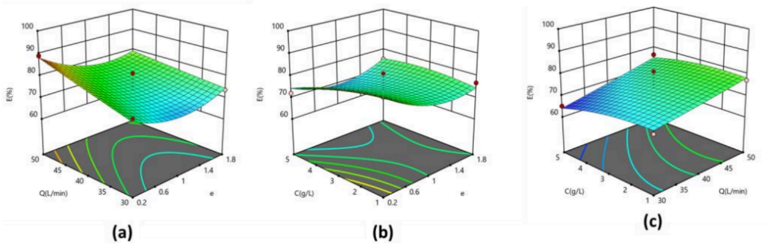

Figure 14. Response surface plot of separation efficiency (a) centrifugal speed/flow rate (b) centrifugal speed/concentration (c) flow rate/concentration

5.3. Pressure field

The internal pressure distribution in a cyclone plays a dual role: it provides energy for particle migration while causing irreversible energy dissipation. As shown in Fig.15, different curved geometries significantly affect the pressure field by altering the flow passage. When the separation space is reduced (e.g., H1), wall static pressure increases, indicating an inverse relationship between space and pressure intensity (H1 > H3). H2 exhibits the highest overall static pressure, mainly due to stronger turbulence dissipation.

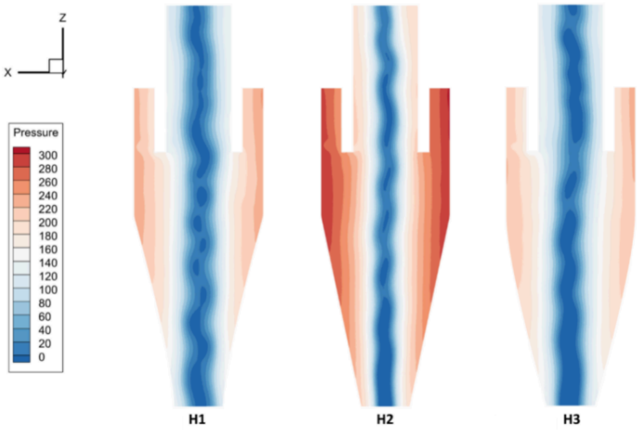

Figure 15. Static pressure field cloud map

5.4. Tangential velocity

In Fig.16, all three cyclones exhibit the typical "forced vortex–free vortex" pattern, but cone profiles lead to distinct flow differences. The concave H1 shows a ~10% higher tangential velocity peak than the straight H2 with slower decay, enhancing fine particle separation. The convex H3 has a smoother distribution and lower decay, sustaining long-range centrifugal motion but with weaker overall force and lower efficiency than H1. The straight H2 shows moderate gradients but notable fluctuations in the transition region, indicating limited flow stability.

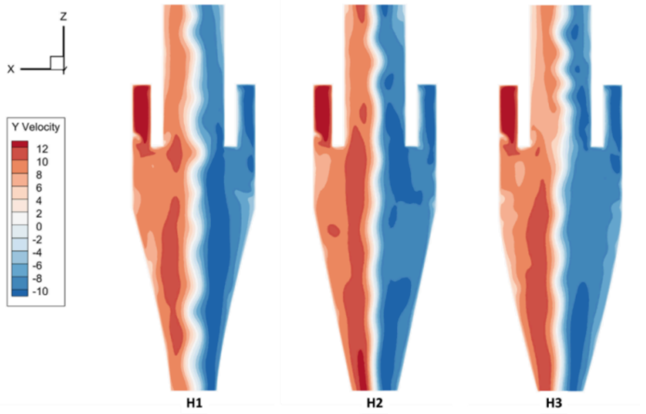

Figure 16. Tangential velocity cloud

5.5. Axial velocity

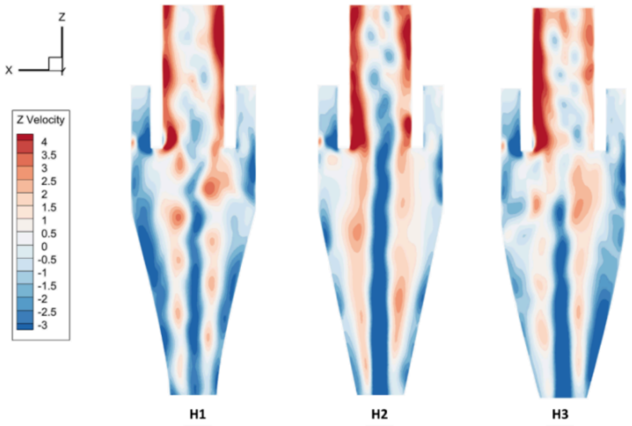

Figure 17. Axial velocity cloud

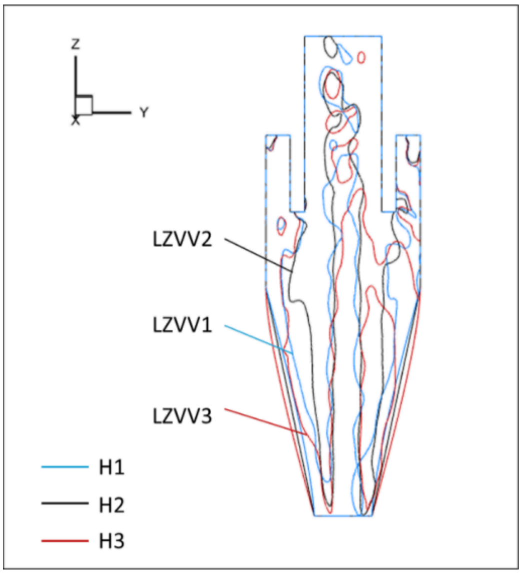

Figure 18. Axial velocity cloud

As shown in Figs.17-18, all three cyclones exhibit similar axial velocity patterns, with a downward outer flow and an upward inner flow separated by the locus of zero vertical velocity (LZVV). In the straight H2, the near-wall axial velocity is too low, hindering particle settling, while excessive upward velocity in the cone promotes particle escape through the overflow, increasing bypass risk.

5.6. Tubulence energy

In Fig.19, all cyclones exhibit high turbulent kinetic energy regions (1.8–2.2 m²/s²) in the cone transition and underflow zones due to flow separation and vortex shedding, which hinders PM2.5 capture. The convex H3 shows the most uniform distribution and smallest high-turbulence region, with ~30% lower near-wall turbulence than H2, suppressing particle diffusion. The straight H2 has peak turbulence at the cone bottom with uneven distribution, causing efficiency fluctuation and back-mixing. The concave H1 is intermediate, as its geometry constrains the flow and reduces disorder.

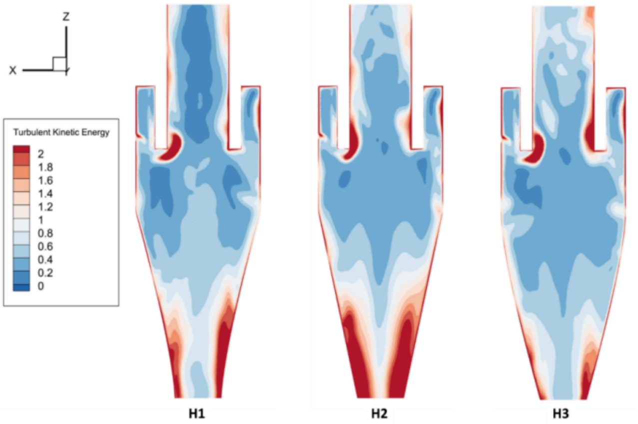

Figure 19. Turbulent kinetic energy cloud map

5.7. Particle track regulation

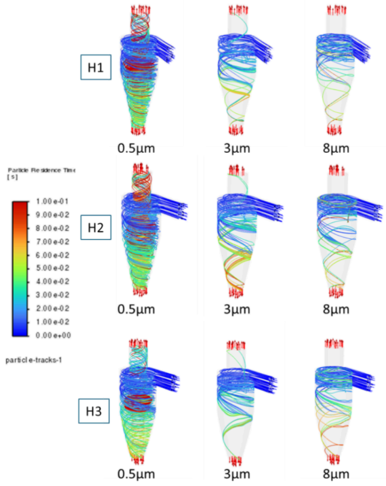

Figure 20. Trajectory diagram of particles in cyclone

As shown in Fig.20, DPM trajectories indicate that separation efficiency increases with particle size, with 8 μm particles fully separated (100%) in all configurations. The straight H2 performs worst for 0.5 μm particles due to stronger flow disturbances causing recirculation and longer residence time, especially in the lower cone. H1 and H3 perform better, with H3 showing the best performance by reducing turbulence, suppressing back-mixing, and enhancing particle migration toward the underflow.

5.8. Fractional efficiency

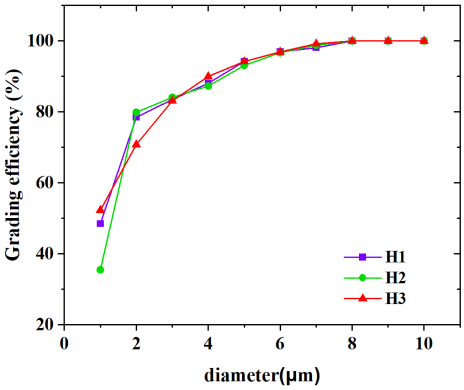

Figure 21. Hierarchy diagram

In Fig. 21, the grade efficiency curve represents the distribution of particles between overflow and underflow, with d50 as a key indicator. Results show that particles larger than 8 μm are fully separated (100%) in all configurations. The straight H2 performs relatively well only in the 2–3 μm range but remains the weakest overall, with lower efficiency than H1 and H3 across most sizes. The convex H3 achieves the highest efficiency near 1 μm (>50%), benefiting from stable high tangential velocity and low turbulence. The concave H1 surpasses H3 around 2 μm and exhibits the best overall efficiency due to stronger centrifugal force and higher tangential velocity. Overall, curve geometry significantly influences classification performance, with distinct advantages across particle size ranges.

6. Conclusion

This study integrates CFD simulations (RSM+DPM) with Box–Behnken response surface experiments, using eccentricity e (0.2–1.8) to parameterize curved cone walls and reveal how curvature enhances PM2.5 separation by regulating velocity gradients, turbulence, and particle trajectories. Results show that the convex design (e=1.8) achieves the best balance, reaching 78% efficiency for 1 μm particles (15% improvement) with reduced pressure drop; the concave design (e=0.2) achieves >85% overall efficiency at high concentrations but with higher energy consumption; the straight cone performs worst due to flow instability. Mechanistically, curved walls optimize tangential velocity, turbulence dissipation, and zero-axial velocity surfaces, improving radial migration and suppressing back-mixing. These designs suit low-energy household and high-load industrial scenarios, providing a basis to overcome HEPA limitations.

References

[1] GB/T 18883-2022.Indoor Air Quality Standard [S].

[2] Wang Qingqin, Li Guozhu, Zhao Li, et al.Current Status, Control Technologies and Standards for Fine Particulate Matter (PM2.5) Pollution in Building Interior [J].HVAC, 2016, 46(2): 1-7.

[3] Zhang Muxu, He Wenzhi, Li Guangming, et al.Microplastic generation and environmental hazards in atmospheric environment [J].Applied Chemical Industry, 2022, 51(10): 3025-3037.

[4] Riederer A M, Krenz J E, Tchong-French M I, Riederer A M, Krenz J E, Tchong-French M I, et al. Effectiveness of portable HEPA air cleaners on reducing indoor PM2.5 and NH3 in an agricultural cohort of children with asthma: a randomized intervention trial [J]. Indoor Air, 2021, 31(2): 454-466.

[5] Jones O, Conway S. The international reach of entrepreneurial social networks: The case of James Dyson in the UK [J]. International entrepreneurship in small and medium size enterprises. Edward Elgar, Cheltenham, op. cit, 2004: 87-106.

[6] Ji L, Paul P, Shanbhag B K, et al.Emerging application of hydrocyclone in biotechnology and food processing [J]. Separation and Purification Technology, 2023, 309: 117629.

[7] Wang J, Bai Z, Yang Q, et al. Investigation of the simultaneous volumetric 3-component flow field inside a hydrocyclone [J].Separation and Purification Technology, 2016, 163: 120-127.

[8] Ni L, Tian J, Song T, et al.Optimizing geometric parameters in hydrocyclones for enhanced separations: a review and perspective [J].Separation & Purification Reviews, 2018, 48(1): 30-51.

[9] Vakamalla T R, Koruprolu V B R, Arugonda R, et al.Development of novel hydrocyclone designs for improved fines classification using multiphase CFD model [J]. Separation and Purification Technology, 2017, 175: 481-497.

[10] Young G, Wakley W, Taggart D, Young G, Wakley W, Taggart D, et al. Oil-water separation using hydrocyclones: an experimental search for optimum dimensions [J]. Journal of Petroleum Science and Engineering, 1994, 11(1): 37-50.

[11] Yang Q, Wang H L, Liu Y, Yang Q, Wang H L, Liu Y, et al. Solid/liquid separation performance of hydrocyclones with different cone combinations [J]. Separation and Purification Technology, 2010, 74(3): 271-279.

[12] Jiang L, Liu P, Yang X, Jiang L, Liu P, Yang X, et al. Comparative classification studies of red mud by using hydrocyclones[J]. Minerals Engineering, 2019, 131: 124-130.

[13] Ghodrat M, Kuang S B, Yu A B, Ghodrat M, Kuang S B, Yu A B, et al. Numerical analysis of hydrocyclones with different conical section designs [J]. Minerals Engineering, 2014, 62: 74-84.

[14] Yu B, Peng Y, Luo X, Yu B, Peng Y, Luo X, et al. Numerical investigation of erosion characteristics of coupling separators with different conical profiles [J]. Chemical Engineering Research and Design, 2022, 188: 790-807.

[15] Liu P, Wang H, Jiang L, et al. Cone structure design for improving the separation performance of a water-only cyclone [J]. Chemical Engineering Research and Design, 2023, 194: 27-40.

[16] Ye J, Xu Y, Song X, et al. Numerical modelling and multi-objective optimization of the novel hydrocyclone for ultra-fine particles classification [J]. Chemical Engineering Science, 2019, 207: 1072-1084.

[17] Pandey S, Brar L S. On the performance of cyclone separators with different shapes of the conical section using CFD [J]. Powder Technology, 2022, 407: 117629.

[18] Li F, Liu P, Yang X, et al. Numerical analysis on the effect of combined-curve tapered segment on the flow field and separation performance of hydrocyclones [J]. Arabian Journal for Science and Engineering, 2021, 47(5): 6193-6207.

[19] Ye J, Xu Y, Song X, et al. Novel conical section design for ultra-fine particles classification by a hydrocyclone [J]. Chemical Engineering Research and Design, 2019, 144: 135-149.

[20] Liu X, Wang J, Wang H, et al. Parametric design of curved hydrocyclone using data points and its separation enhancement mechanism [J]. Chemical Engineering and Processing: Process Intensification, 2024, 205: 110043.

[21] Pukkella A K, Cilliers J, Hadler K. Design of parabolic conic gas cyclones for coarse particle classification: A CFD study with Response Surface Methodology [J]. Powder Technology, 2024, 433: 119217.